ARTICLE OPEN

Check for updates

Pseudogap behavior in charge density wave kagome material ScV_6Sn_6 revealed by magnetotransport measurements

Jonathan M. DeStefano[1], Elliott Rosenberg[1], Olivia Peek[1], Yongbin Lee[2], Zhaoyu Liu[1], Qianni Jiang[1], Liqin Ke[2] and Jiun-Haw Chu[1]✉

Over the last few years, significant attention has been devoted to studying the kagome materials $A\,V_3Sb_5$ (A = K, Rb, Cs) due to their unconventional superconductivity and charge density wave (CDW) ordering. Recently ScV_6Sn_6 was found to host a CDW below ≈ 90 K, and, like $A\,V_3Sb_5$, it contains a kagome lattice comprised only of V ions. Here we present a comprehensive magnetotransport study on ScV_6Sn_6. We discovered several anomalous transport phenomena above the CDW ordering temperature, including insulating behavior in interlayer resistivity, a strongly temperature-dependent Hall coefficient, and a violation of Kohler's rule. All these anomalies can be consistently explained by a progressive decrease in carrier densities with decreasing temperature, suggesting the formation of a pseudogap. Our findings suggest that high-temperature CDW fluctuations play a significant role in determining the normal state electronic properties of ScV_6Sn_6.

npj Quantum Materials (2023)8:65 ; https://doi.org/10.1038/s41535-023-00600-8

INTRODUCTION

Materials containing kagome lattices have emerged as a promising platform for studying the interplay of electronic correlations and topology[1–4]. Among these, kagome metals hosting charge density waves have gained significant attention due to their symmetry-breaking phases and rich phase diagrams[5–7]. The $A\,V_3Sb_5$ (A = K, Rb, Cs) family hosts a charge density wave (CDW) with T_{CDW} at ≈80 K. Although controversies remain[8], the CDW potentially breaks time-reversal symmetry[9] and rotational symmetry[10–12], leading to speculation about an orbital current loop state[13–15] and electronic nematicity[16]. At lower temperatures (<3 K), a superconducting state coexists and competes with the CDW[6,7,17], displaying signatures of a pair density wave[18]. Many of these phenomena resemble the characteristics of other strongly correlated systems, such as high-temperature superconductors, where the extended fluctuation regime gives rise to intertwined orders and complex phase diagrams[19].

ScV_6Sn_6 is the latest addition to the set of kagome metals exhibiting CDWs, with a CDW transition temperature near 90 K[20]. Since this compound contains kagome layers comprised solely of V ions, it is natural to compare it to the $A\,V_3Sb_5$ family. However, early studies have found several distinct differences between ScV_6Sn_6 and these compounds. In ScV_6Sn_6 the CDW is associated with a $\sqrt{3} \times \sqrt{3}$ in-plane ordering[20], which is different from the 2×2 ordering in $A\,V_3Sb_5$ where the wave vectors nest the van Hove singularities of the kagome-derived energy bands. In ScV_6Sn_6 the lattice distortion associated with the CDW is mostly along the c-axis[20] whereas the distortion in $A\,V_3Sb_5$ is mostly in the ab-plane[21]. Unlike the $A\,V_3Sb_5$ family, no superconductivity has been found in ScV_6Sn_6 down to 40 mK even under high pressures[22]. Nevertheless, similar to the $A\,V_3Sb_5$ family, signatures of time-reversal symmetry breaking have been suggested by muon spin relaxation rate measurements and a potential anomalous Hall effect[23–25]. Recent measurements, including scanning tunneling microscopy, angle-resolved photoemission spectroscopy, and Raman spectroscopy suggest the CDW is primarily structurally driven[26–28], resulting from the softening of a multitude of phonon modes[29–31], indicating a minor role of the electronic degrees of freedom in the CDW formation. However, despite the first-order nature of the CDW transition, recent studies have revealed short-range CDW fluctuations persisting well above T_{CDW} in ScV_6Sn_6[29,30,32]. Hence, it is crucial to examine whether these fluctuations impact the electronic properties, as observed in other strongly correlated systems.

In this paper, we present evidence of a pseudogap above the CDW transition in ScV_6Sn_6. Pseudogap formation was first observed in the cuprate superconducting family, and it refers to the suppression of the density of states which was revealed by various spectroscopy measurements and anomalous transport behavior[33]. Our conclusion of pseudogap formation in ScV_6Sn_6 is established from a comprehensive magnetotransport study, including measurements of the interlayer resistivity, magnetoresistance, and the Hall effect, all consistent with an abnormal decrease of carrier density with decreasing temperature above the CDW transition. In addition, we found several striking similarities to the proposed pseudogap phase in the Fe-based superconductors, in which strong spin density wave fluctuations persist well above the transition temperature. Our results suggest that there is an extended fluctuation regime in ScV_6Sn_6 which strongly influences the electronic transport properties above the transition temperature.

RESULTS

Zero-field resistivity

Figure 1 presents in-plane resistivity, ρ_{xx}, and interlayer resistivity, ρ_{zz} (divided by 5), of a typical ScV_6Sn_6 sample as a function of temperature while cooling. ρ_{xx} is consistent with previous reports[20,22], with residual resistivity ratios of various samples ranging from 3 to 10. Drops in resistivity are present in both curves near 90 K, indicating the charge density wave transition (T_{CDW})[20]. It should be noted that this is a first-order transition, but only the cooling curve is shown due to the small temperature hysteresis of this transition (≈1–2 K). As previously noted[22], charge

[1]Department of Physics, University of Washington, Seattle, WA 98112, USA. [2]Ames Laboratory, U.S. Department of Energy, Ames, IA 50011, USA. ✉email: jhchu@uw.edu

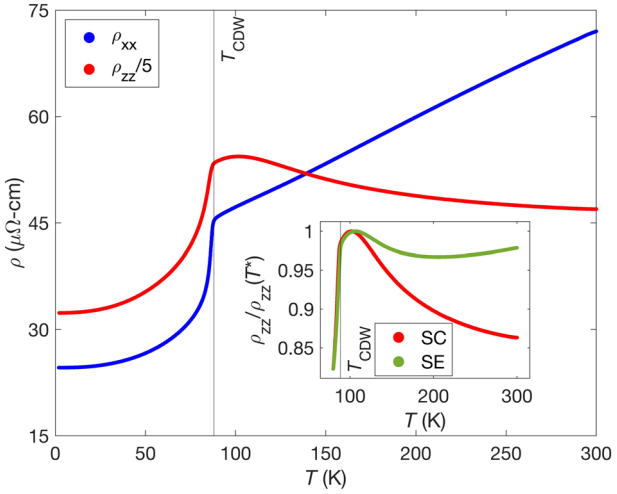

Fig. 1 Resistivity vs. temperature for ScV_6Sn_6. ρ_{xx} and ρ_{zz} (divided by 5) of ScV_6Sn_6 as a function of temperature. T_{CDW} is marked with a vertical line. Inset: ρ_{zz} of two different samples each normalized to be 1 at T^* as discussed in the main text. Here "SC" and "SE" refer to Sample C and Sample E, respectively. T_{CDW} is marked in the same way as the main figure.

density wave phase transitions in layered materials typically appear as hump-like increases in resistivity as a function of temperature, as parts of the Fermi surface get gapped out by the transition.

The drop of resistivity at T_{CDW} is reminiscent of the spin density wave transition in the parent compounds of the iron pnictide superconductors, such as $BaFe_2As_2$, which is also characterized by a similar feature[34]. This unusual behavior in $BaFe_2As_2$ is understood as a more rapid decrease of scattering rates relative to the decrease of carrier density below the spin density wave transition. Like observed in $BaFe_2As_2$, optical measurements of ScV_6Sn_6[35] have also revealed a similar decrease in both the carrier density and the scattering rate below T_{CDW}, which could explain the increase in conductivity. The enhanced electron scattering above T_{CDW} can be explained by the competing CDW fluctuations above T_{CDW}[32].

The interlayer resistivity measurements reveal a moderate resistivity anisotropy in ScV_6Sn_6 with ρ_{zz} roughly 5 times larger than ρ_{xx} at 2 K. This is considerably smaller than in CsV_3Sb_5 where ρ_{zz} is ≈20 times larger than ρ_{xx} at low temperatures[10], implying ScV_6Sn_6 is more 3-dimensional than CsV_3Sb_5. Nevertheless, unlike CsV_3Sb_5, the temperature dependence of ρ_{zz} is dramatically different from ρ_{xx}, showing a broad maximum of roughly 15 K above T_{CDW} at T^*. As shown in the inset of Fig. 1, for temperatures above T^* multiple ScV_6Sn_6 samples display insulating behavior (here "SC" and "SE" refer to Sample C and Sample E, respectively. A summary of the samples measured can be found in Supplementary Table 2). The difference in high-temperature resistivity between samples may be explained by contamination from lower resistivity in-plane components.

The insulating interlayer resistivity and metallic in-plane resistivity have been observed in highly anisotropic layered materials such as Sr_2RuO_4, in which the much weaker interlayer tunneling results in incoherent c-axis transport[36]. However, such a phenomenon is usually seen in materials with resistivity anisotropy $\rho_{zz}/\rho_{xx} \gg 10$, which is not applicable to ScV_6Sn_6 where $\rho_{zz}/\rho_{xx} \approx 5$. Interestingly, a similar insulating temperature dependence with a broad maximum in ρ_{zz} above a density wave transition has also been observed in $BaFe_2As_2$[34,37–40], which also has a moderate resistivity anisotropy ($\rho_{zz}/\rho_{xx} \approx 7$). The insulating ρ_{zz} in $BaFe_2As_2$ was interpreted as a signature of a pseudogap, resulting from the spin density wave fluctuations partially gapping the section of the Fermi surface where the Fermi velocity has a large z-component. We propose that a similar mechanism could be responsible for the insulating ρ_{zz} in ScV_6Sn_6, which is further supported by the Hall effect and magnetoresistance analysis presented in the following sections.

Hall effect

Figure 2a presents ρ_{xy} as a function of the magnetic field at a variety of temperatures. These data are taken from Sample A which has a RRR of 6.0 and T_{CDW} of 93 K (a summary of T_{CDW} and RRR of the samples measured can be found in Supplementary Table 2). Across the entire measured temperature range ρ_{xy} is non-linear, but while it evolves smoothly as a function of temperature above T_{CDW}, it stays relatively unchanged below T_{CDW}. There are two possible sources for the non-linearity in ρ_{xy}: the multi-band effect and the anomalous Hall effect. We first present an analysis of fitting of ρ_{xy} using a two-band model, which reveals a strong temperature dependence of carrier density above the CDW transition. We will also argue that this conclusion can be made from the high field Hall coefficient of ρ_{xy} even without any two-band fitting.

In order to analyze the two-band Hall effect, the standard two-band model is used to simultaneously fit $\rho_{xx}(\mu_0 H)$ and $\rho_{xy}(\mu_0 H)$ at each temperature[41]. The carrier densities and mobilities were determined by a non-linear least squares minimization of the error $(\rho_{xy}-\rho_{xy}^{fit})^2 + C(\rho_{xx}-\rho_{xx}^{fit})^2$ where C provided a weighting such that ρ_{xy} was prioritized (as ρ_{xx} has potentially more scattering contributions than those arising from the two-band model). Figure 2b shows the fits to ρ_{xy} at 150 and 3 K. Above T_{CDW} the two-band model fits ρ_{xy} well, but below T_{CDW} the two-band fit loses quality, particularly in the low field regime. This disagreement may be due to the contribution from an anomalous Hall effect[24,25]. Figure 2c and d present the carrier densities and mobilities, respectively, that are extracted from the two-band fitting. It should be noted that the quantitative values below T_{CDW} should not be taken as exact due to the decrease in fit quality in ρ_{xy}. At all temperatures, n_h is greater than n_e by several orders of magnitude. Notably, above T_{CDW} n_h decreases significantly, although n_e is roughly constant, and below T_{CDW} n_h is roughly constant while n_e grows by several times. Both μ_e and μ_h increase as temperature decreases which is typical for a metal.

Due to the substantial deviation from the two-band model of the Hall data below T_{CDW}, we estimate the carrier density using the Hall data in the high field limit in two more ways to ensure our conclusions are robust. First, the Hall coefficient, $R_H = \frac{\rho_{xy}}{\mu_0 H}$, should saturate to $\frac{1}{(n_h - n_e)e}$ at the high field limit where e is the charge of an electron[42]. These data are shown in Fig. 3a. The blue data in Fig. 3c present the extracted $n_h - n_e$ from the high field Hall coefficient. Second, the red data in Fig. 3c show n_h using $\frac{d\rho_{xy}}{d\mu_0 H}$ ($\mu_0 H = 14$ T) $\approx \frac{1}{n_h e} \cdot \frac{d\rho_{xy}}{d\mu_0 H}$ as a function of magnetic field is shown in Fig. 3b. This method provides an estimate of carrier density even when the low-field data can not be well represented by the two-band model. While the three methodologies used to estimate the carrier densities vary quantitatively, they are all of the same order of magnitude and qualitatively consistent—above T_{CDW} the number of holes decreases as a function of temperature, and below T_{CDW} the number of holes is roughly constant.

Magnetoresistance (MR) and Kohler's rule analysis

The ab-plane MR ($MR_{xx} = \frac{\Delta\rho_{xx}}{\rho_{xx}(\mu_0 H=0)} * 100\%$) with a c-axis magnetic field at various temperatures is shown in Fig. 4a. These data are from Sample B which has a RRR of 4.3 and two drops in the resistivity at 80 and 88 K. This apparent double transition at T_{CDW} in ρ_{xx} has been noted before[24], and the meaning of this feature is

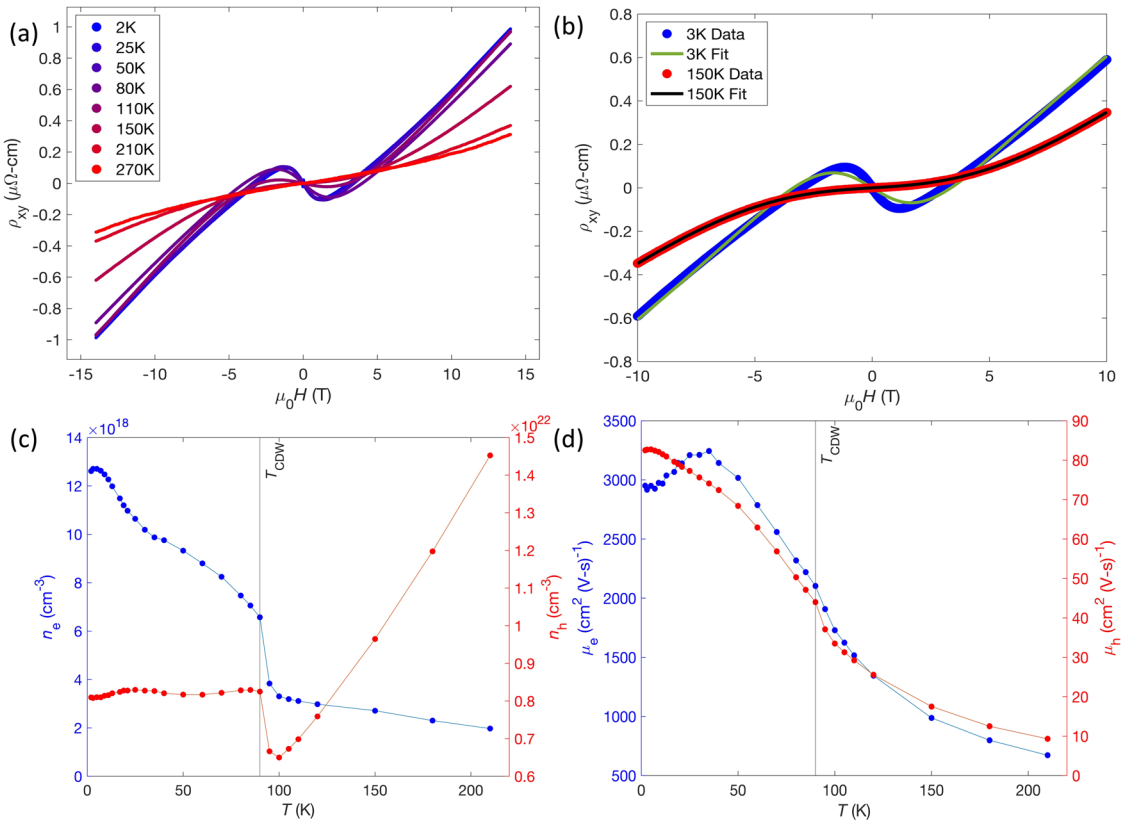

Fig. 2 Hall effect and two-band analysis. a ρ_{xy} as a function of magnetic field at various temperatures. **b** ρ_{xy} as a function of magnetic field at 3 and 150 K with fits to the two-band model. **c** n_e and n_h as a function of temperature extracted from fits to the two-band model. **d** μ_e and μ_h as a function of temperature extracted from fits to the two-band model.

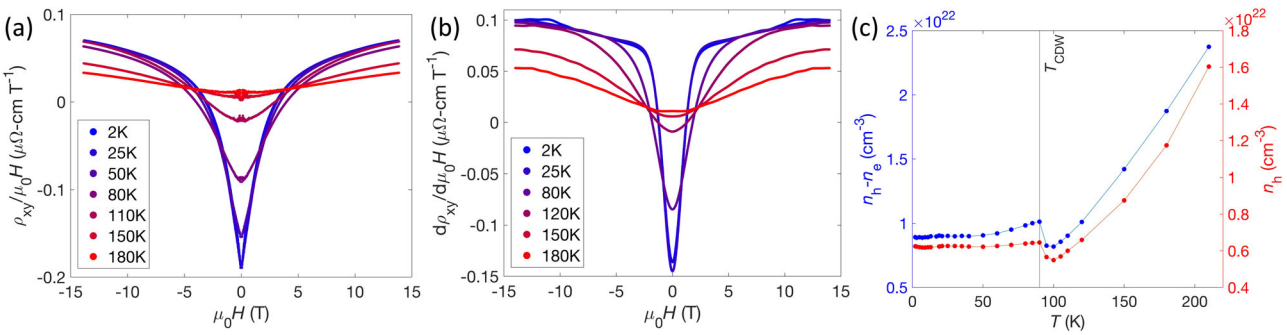

Fig. 3 High field limit Hall analysis. a $\frac{\rho_{xy}}{\mu_0 H}$ as a function of $\mu_0 H$ to evaluate the high field limit of the two-band model. Note that the curves are not fully saturated at 14 T. **b** $\frac{d\rho_{xy}}{d\mu_0 H}$ as a function of $\mu_0 H$ to approximate the carrier concentration using a one-band model. **c** $n_h - n_e$ extracted from the high field limit of the two-band model and n_h from the high field regime of a one-band model. While quantitatively different than the results presented in Fig. 2 for reasons described in the main text, all three of these analyses are qualitatively consistent.

not yet understood. This MR looks qualitatively similar to that observed in the *A* V_3Sb_5 family in that the low field behavior shows a cusp at low temperatures and evolves to a more standard quadratic behavior at high temperatures[43]. At low temperatures quantum oscillations can be resolved once a background subtraction is performed. The *c*-axis magnetoresistance (MR_{zz}) with a magnetic field in the ab-plane at several temperatures is presented in Fig. 4b. These data are from Sample C which has a T_{CDW} of 86 K. The MR_{zz} of another sample was measured and was similar to the data presented here. While MR_{zz} looks qualitatively similar to MR_{xx}, MR_{zz} is about double the size at 2 K. Also, at low temperatures quantum oscillations are observed much more prominently in MR_{zz}. These quantum oscillations, as well as accompanying electronic structure calculations, are discussed in Supplemental Note 1 and are in agreement with a very recent study[25]. Overall, the quantum oscillations reveal three-dimensional Fermi pockets occupying less than a percent of the Brillouin zone with effective masses between 0.1 and 0.2m_0 (the free electron mass). These pockets are consistent with the high mobility and low density of electron carriers extracted from the two-band Hall fitting.

Kohler's rule of magnetoresistance[44] is violated in ScV_6Sn_6 as shown in Fig. 5a as MR_{xx} is not simply a function of $\mu_0 H/\rho_{xx,0}$ where $\rho_{xx,0}$ is the zero-field resistivity. It should be noted that the data point spread at low fields and high temperatures is due to the small MR in this regime. The violation of Kohler's rule in ScV_6Sn_6

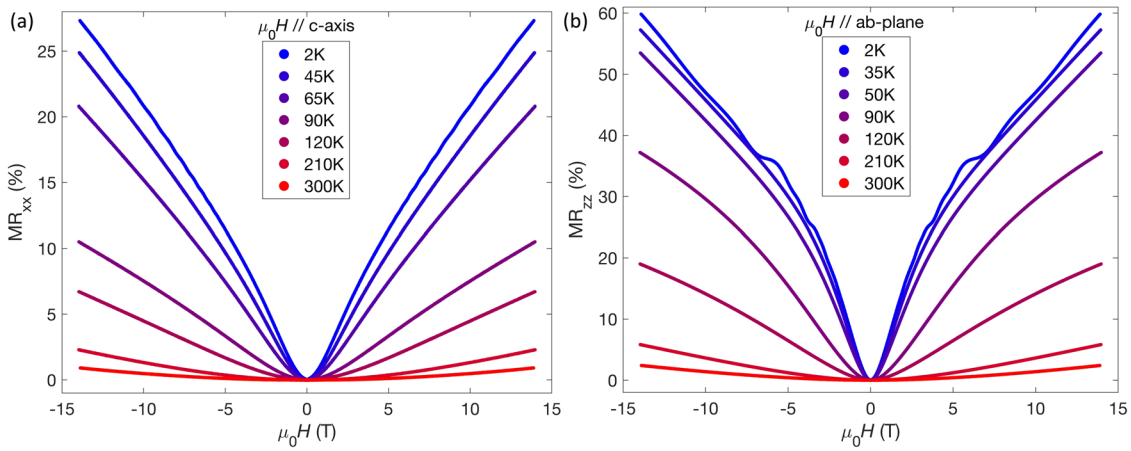

Fig. 4 Magnetoresistance of ScV_6Sn_6. a MR_{xx} as a function of the magnetic field at various temperatures. **b** Magnetic field dependence of MR_{zz} at several temperatures.

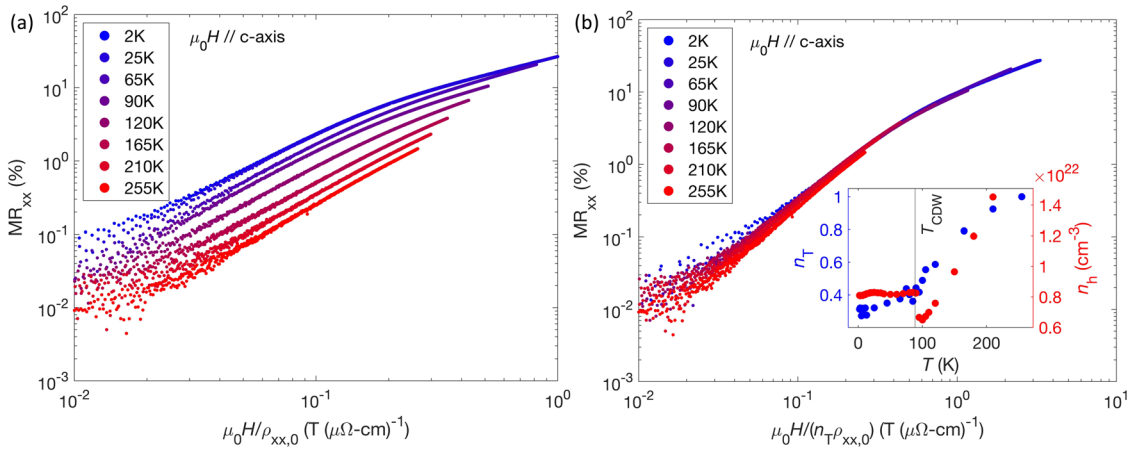

Fig. 5 Kohler's rule analysis of ScV_6Sn_6. a MR_{xx} as a function of $\mu_0H/\rho_{xx,0}$ using the data from Fig. 4a on a log–log scale. Kohler's rule is violated as the data from different temperatures do not collapse onto each other. **b** Extended Kohler's rule applied to the same data as presented in **a** by plotting MR_{xx} as a function of $\mu_0H/(n_T\rho_{xx,0})$ on a log–log scale. Inset: extracted n_T as a function of temperature. n_h extracted from the two-band Hall fitting as discussed in the section "Hall effect" is also plotted in the inset to highlight the similar temperature dependencies between n_h and n_T.

was also reported in a recent study[23]. Similar violations of Kohler's rule have been used as evidence of phase transitions[45] or non-Fermi liquid behavior[46,47]. Recently, an extended Kohler's rule has been developed[48] in which the MR is expressed as a function of $\mu_0H/(n_T\rho_{xx,0})$ where n_T describes the relative change in the carrier density. The extended Kohler's rule successfully explains the violation of conventional Kohler's rule by incorporating a temperature-dependent carrier density, which could arise from a phase transition that partially gaps the Fermi surfaces or thermal excitations in topological semimetals where the Fermi energy is comparable to k_BT[48]. Here we apply this formula with n_T fixed to be 1 at 255 K to collapse the MR curves onto the linear part of the 255 K MR (Fig. 5b). Through this method, n_T can be extracted as a function of temperature, and is presented in the inset of Fig. 5b. Intriguingly, Kohler's rule is nearly followed below T_{CDW} as evidenced by the nearly constant value of n_T, but above this temperature Kohler's rule is clearly violated. These results are consistent with those presented in the section "Hall effect"—n_h extracted from two-band fitting is also plotted in the inset of Fig. 5b to show the similar behavior between the concentration of the dominant carriers (holes) and n_T, as both decrease above T_{CDW} and become relatively constant below T_{CDW}. Analysis of MR_{zz} data using the extended Kohler's rule yields similar results to that of MR_{xx}: above T_{CDW} n_T decreases quickly with decreasing temperature, and below T_{CDW} n_T changes far less drastically. These data are presented in Supplementary Note 2.

DISCUSSION

Both Kohler's rule analysis and the Hall effect demonstrate a pronounced temperature dependence of the carrier density in ScV_6Sn_6, decreasing by almost a factor of 2 from the value at 200 K to the value just above the CDW transition temperature $T_{CDW} = 90$ K. This decrease in carrier density is consistent with the insulating temperature dependence observed in interlayer resistivity. Interestingly, similar characteristics have also been observed in Fe-based superconductors, such as $BaFe_2As_2$. The temperature dependence of in-plane and interlayer resistivity, as well as the resistivity anisotropy ratio, exhibit a remarkable resemblance between $BaFe_2As_2$ and ScV_6Sn_6[34]. Additionally, in $BaFe_2As_2$ the Hall coefficient also shows a substantial increase with decreasing temperature above the spin density wave transition[49–51]. This is also seen in the pseudogap regime of the cuprate superconductors[52]. Another striking similarity can be observed in the magnetic susceptibilities of $BaFe_2As_2$ and ScV_6Sn_6 (presented in ref. [20]). In both materials there is a drop in the susceptibility at the phase transition, but these potentially stem from different mechanisms, for in $BaFe_2As_2$ this is likely due to

enhanced magnetic correlations. Also in both materials, the susceptibility shows a linear increase with increasing temperature above the phase transition, which cannot be explained by either Pauli paramagnetic susceptibility or Curie Weiss susceptibility[53,54].

In $BaFe_2As_2$, the anomalous transport and magnetic properties observed above the transition temperature have been attributed to strong spin density wave fluctuations. However, in the case of ScV_6Sn_6, the CDW transition is first-order, which could explain the nearly temperature-independent carrier density below T_{CDW}, but contradicts with the existence of an extended fluctuation regime above T_{CDW}. Nevertheless, theoretical studies have suggested that, in addition to the long-range $\sqrt{3} \times \sqrt{3} \times 3$ CDW that develops below T_{CDW}, there are several other nearly degenerate CDW instabilities associated with different ordering wave vectors[29]. Furthermore, experimental evidence has shown the presence of a short-range $\sqrt{3} \times \sqrt{3} \times 2$ CDW well above T_{CDW}, which is suppressed by the $\sqrt{3} \times \sqrt{3} \times 3$ CDW through a first-order transition at T_{CDW}[32]. It is possible that the short-range CDW fluctuations are responsible for the anomalous decrease of carrier density and insulating interlayer resistivity observed in ScV_6Sn_6.

It should be noted that a pseudogap in the $BaFe_2As_2$ family has been identified using a variety of techniques including angle-resolved photoemission spectroscopy (ARPES)[55] and optical conductivity[56]. While several works have presented ARPES[26,28,57,58] and scanning tunneling microscopy[26,58] data on ScV_6Sn_6, to our knowledge no measurements were performed above 120 K. Thus, it is possible that future studies will reveal a pseudogap in this material using these experimental probes.

In conclusion, the transport behavior in the normal state of ScV_6Sn_6 is consistent with the formation of a pseudogap, which is likely arising from high-temperature CDW fluctuations. We have also highlighted several similarities between ScV_6Sn_6 and Fe-based superconductors with pseudogaps above their ordering temperatures. Due to the high degree of tunability in the RT_6X_6 family (R = rare earth, T = transition metal, X = Si, Ge, Sn), ScV_6Sn_6 offers an exciting platform to study exotic electronic ordering in a kagome material.

Note: During the preparation of this paper we became aware of a separate study that reported the two-band behavior of the Hall effect in ScV_6Sn_6[24]. They discovered high carrier density and low mobility holes and low carrier density and high mobility electrons, which broadly corroborates our findings.

METHODS

Sample preparation

Single crystals of ScV_6Sn_6 were grown using a flux method similar to the one previously reported[20]. Mixtures of Sc pieces (99.9%), V pieces (99.9%), and Sn shot (99.999%) were loaded into Canfield crucible sets[59] with atomic ratios 1:3:30, then vacuum-sealed in quartz tubes. These were heated to 1150 °C in 12 h, held at this temperature for 15 h, then cooled to 780 °C in 200 h where the growths were decanted in a centrifuge to separate the excess flux from the single crystals. Dilute HCl was used to etch the remaining flux from the surface of the crystals. The phase of the crystals was confirmed using energy-dispersive X-ray spectroscopy with a Sirion XL30 scanning electron microscope. The orientation of the crystallographic axes was determined using a Rigaku MiniFlex 600 system, with a Cu source and Hy-Pix 400MF 2D detector.

Transport measurements

Transport measurements were performed on samples that were polished and cut by a wire saw to be bar-shaped with dimensions roughly 1 mm × 0.4 mm × 0.05 mm (in-plane current) or 0.2 mm × 0.15 mm × 0.05 mm (out-of-plane current). Silver paste or two-part silver epoxy (H20-E) and gold wires were used to make 4-point and 5-point (Hall pattern) measurements. These measurements were performed in a Quantum Design Dynacool Physical Property Measurement System with standard lock-in techniques in temperatures ranging from 1.7 to 300 K and in magnetic fields up to 14 T. To eliminate any contributions from contact misalignment, the in-line and Hall resistivities were symmetrized and anti-symmetrized, respectively. For some of the measurements, the samples were rotated in situ using a Quantum Design in-plane rotator.

Density functional theory calculations

Density functional theory (DFT) calculations were performed using a full-potential linear augmented plane wave (FP-LAPW) method, as implemented in WIEN2K[60]. The primitive cell contains one formula unit, and experimental lattice parameters[20] were adopted. The generalized gradient approximation of Perdew et al.[61] was used for the correlation and exchange potentials. To generate the self-consistent potential and charge, we employed $R_{MT} \cdot K_{max} = 8.0$ with Muffin–Tin (MT) radii $R_{MT} = 2.4$, 2.4, and 2.5 a.u., for Sc, V, and Sn, respectively. The self-consistent calculations were performed with 490 k-points in the irreducible Brillouin zone (BZ). They were iterated until charge differences between consecutive iterations were $<1 \times 10^{-3}e$ and the total energy difference lower than 0.01 mRy. After obtaining a self-consistent charge, band energies were calculated with a $64 \times 64 \times 33$ fine k-mesh for the full Brillouin Zone (FBZ).

We employed FermiSurfer[62] and SKEAF[63] for visualizing FS and calculating de Haas–van Alphen (dHvA) frequencies, respectively.

DATA AVAILABILITY

All data supporting the findings of this study are available upon request.

Received: 16 June 2023; Accepted: 23 October 2023;
Published online: 06 November 2023

REFERENCES

1. Kuroda, K. et al. Evidence for magnetic weyl fermions in a correlated metal. *Nat. Mater.* **16**, 1090–1095 (2017).
2. Ye, L. et al. Massive dirac fermions in a ferromagnetic kagome metal. *Nature* **555**, 638–642 (2018).
3. Kang, M. et al. Topological flat bands in frustrated kagome lattice CoSn. *Nat. Commun.* **11**, 4004 (2020).
4. Yin, J.-X. et al. Quantum-limit Chern topological magnetism in $TbMn_6Sn_6$. *Nature* **583**, 533–536 (2020).
5. Teng, X. et al. Discovery of charge density wave in a kagome lattice antiferromagnet. *Nature* **609**, 490–495 (2022).
6. Yin, Q. et al. Superconductivity and normal-state properties of Kagome metal RbV_3Sb_5 single crystals. *Chin. Phys. Lett.* **38**, 037403 (2021).
7. Zhao, H. et al. Cascade of correlated electron states in the kagome superconductor CsV_3Sb_5. *Nature* **599**, 216–221 (2021).
8. Saykin, D. R. et al. High resolution polar Kerr effect studies of CsV_3Sb_5: tests for time-reversal symmetry breaking below the charge-order transition. *Phys. Rev. Lett.* **131**, 016901 (2023).
9. Mielke, C. et al. Time-reversal symmetry-breaking charge order in a kagome superconductor. *Nature* **602**, 245–250 (2022).
10. Xiang, Y. et al. Twofold symmetry of c-axis resistivity in topological kagome superconductor CsV_3Sb_5 with in-plane rotating magnetic field. *Nat. Commun.* **12**, 6727 (2021).
11. Xu, Y. et al. Three-state nematicity and magneto-optical Kerr effect in the charge density waves in kagome superconductors. *Nat. Phys.* **18**, 1470–1475 (2022).
12. Li, H. et al. Rotation symmetry breaking in the normal state of a kagome superconductor KV_3Sb_5. *Nat. Phys.* **18**, 265–270 (2022).
13. Feng, X., Jiang, K., Wang, Z. & Hu, J. Chiral flux phase in the Kagome superconductor AV_3Sb_5. *Sci. Bull.* **66**, 1384–1388 (2021).
14. Denner, M. M., Thomale, R. & Neupert, T. Analysis of charge order in the kagome metal AV_3Sb_5 (A = K, Rb, Cs). *Phys. Rev. Lett.* **127**, 217601 (2021).
15. Lin, Y.-P. & Nandkishore, R. M. Complex charge density waves at van Hove singularity on hexagonal lattices: Haldane-model phase diagram and potential realization in the kagome metals AV_3Sb_5 (A = K, Rb, Cs). *Phys. Rev. B* **104**, 045122 (2021).

16. Nie, L. et al. Charge-density-wave-driven electronic nematicity in a kagome superconductor. *Nature* **604**, 59–64 (2022).
17. Ortiz, B. R. et al. Superconductivity in the Z_2 kagome metal KV_3Sb_5. *Phys. Rev. Mater.* **5**, 034801 (2021).
18. Chen, H. et al. Roton pair density wave in a strong-coupling kagome superconductor. *Nature* **599**, 222–228 (2021).
19. Fradkin, E., Kivelson, S. A. & Tranquada, J. M. Colloquium: theory of intertwined orders in high temperature superconductors. *Rev. Mod. Phys.* **87**, 457–482 (2015).
20. Arachchige, H. W. S. et al. Charge density wave in Kagome Lattice Intermetallic ScV_6Sn_6. *Phys. Rev. Lett.* **129**, 216402 (2022).
21. Ortiz, B. R. et al. Fermi surface mapping and the nature of charge-density-wave order in the Kagome superconductor CsV_3Sb_5. *Phys. Rev. X* **11**, 041030 (2021).
22. Zhang, X. et al. Destabilization of the charge density wave and the absence of superconductivity in ScV_6Sn_6 under high pressures up to 11 GPa. *Materials* **15**, 7372 (2022).
23. Guguchia, Z. et al. Hidden magnetism uncovered in charge ordered bilayer kagome material ScV_6Sn_6. Preprint at https://arxiv.org/abs/2304.06436 (2023).
24. Mozaffari, S. et al. Universal sublinear resistivity in vanadium kagome materials hosting charge density waves. Preprint at https://arxiv.org/abs/2305.02393 (2023).
25. Yi, C. et al. Charge density wave induced anomalous Hall effect in kagome ScV_6Sn_6. Preprint at https://arxiv.org/abs/2305.04683 (2023).
26. Cheng, S. et al. Nanoscale visualization and spectral fingerprints of the charge order in ScV_6Sn_6 distinct from other kagome metals. Preprint at https://arxiv.org/abs/2302.12227 (2023).
27. Tuniz, M. et al. Dynamics and resilience of the charge density wave in a bilayer kagome metal. Preprint at https://arxiv.org/abs/2302.10699 (2023).
28. Hu, Y. et al. Phonon promoted charge density wave in topological kagome metal ScV_6Sn_6. Preprint at https://arxiv.org/abs/2304.06431 (2023).
29. Tan, H. & Yan, B. Abundant Lattice Instability in Kagome metal ScV_6Sn_6. *Phys. Rev. Lett.* **130**, 266402 (2023).
30. Korshunov, A. et al. Softening of a flat phonon mode in the kagome ScV_6Sn_6. *Nat. Commun.* **14**, 6646 (2023).
31. Hu, H. et al. Kagome materials I: SG 191, ScV_6Sn_6. Flat phonon soft modes and unconventional CDW formation: microscopic and effective theory. Preprint at https://arxiv.org/abs/2305.15469 (2023).
32. Cao, S. et al. Competing charge-density wave instabilities in the kagome metal ScV_6Sn_6. Preprint at https://arxiv.org/abs/2304.08197 (2023).
33. Timusk, T. & Statt, B. The pseudogap in high-temperature superconductors: an experimental survey. *Rep. Prog. Phys.* **62**, 61 (1999).
34. Tanatar, M. A. et al. Pseudogap and its critical point in the heavily doped $Ba(Fe_{1-x}Co_x)_2As_2$ from *c*-axis resistivity measurements. *Phys. Rev. B* **82**, 134528 (2010).
35. Hu, T. et al. Optical spectroscopy and band structure calculations of the structural phase transition in the vanadium-based kagome metal ScV_6Sn_6. *Phys. Rev. B* **107**, 165119 (2023).
36. Tyler, A. W., Mackenzie, A. P., NishiZaki, S. & Maeno, Y. High-temperature resistivity of Sr_2RuO_4: bad metallic transport in a good metal. *Phys. Rev. B* **58**, R10107–R10110 (1998).
37. Tanatar, M. A. et al. Interplane resistivity of isovalent doped $BaFe_2(As_{1-x}P_x)_2$. *Phys. Rev. B* **87**, 104506 (2013).
38. Tanatar, M. A. et al. Systematics of the temperature-dependent interplane resistivity in $Ba(Fe_{1-x}M_x)_2As_2$ (M = Co, Rh, Ni, and Pd). *Phys. Rev. B* **84**, 014519 (2011).
39. Tanatar, M. A. et al. Interplane resistivity of underdoped single crystals $(Ba_{1-x}K_x)Fe_2As_2$ ($0 \le x < 0.34$). *Phys. Rev. B* **89**, 144514 (2014).
40. Tanatar, M. A. et al. Effects of isovalent substitution and pressure on the interplane resistivity of single-crystal $Ba(Fe_{1-x}Ru_x)_2As_2$. *Phys. Rev. B* **90**, 104518 (2014).
41. Watts, S. M., Wirth, S., von Molnár, S., Barry, A. & Coey, J. M. D. Evidence for two-band magnetotransport in half-metallic chromium dioxide. *Phys. Rev. B* **61**, 9621–9628 (2000).
42. Pippard, A. B. *Magnetoresistance in Metals* (Cambridge University Press, 1988).
43. Yang, S.-Y. et al. Giant, unconventional anomalous Hall effect in the metallic frustrated magnet candidate, KV_3Sb_5. *Sci. Adv.* **6**, eabb6003 (2020).
44. Kohler, M. Zur magnetischen Widerstandsänderung reiner Metalle. *Ann. Phys.* **424**, 211–218 (1938).
45. Wu, Y. et al. Temperature-induced Lifshitz transition in WTe_2. *Phys. Rev. Lett.* **115**, 166602 (2015).
46. Harris, J. M. et al. Violation of Kohler's rule in the normal-state magnetoresistance of $YBa_2Cu_3O_{7-\delta}$ and $La_2Sr_xCuO_4$. *Phys. Rev. Lett.* **75**, 1391–1394 (1995).
47. Kontani, H. Anomalous transport phenomena in Fermi liquids with strong magnetic fluctuations. *Rep. Prog. Phys.* **71**, 026501 (2008).
48. Xu, J. et al. Extended Kohler's rule of magnetoresistance. *Phys. Rev. X* **11**, 041029 (2021).
49. Rullier-Albenque, F., Colson, D., Forget, A. & Alloul, H. Hall effect and resistivity study of the magnetic transition, carrier content, and fermi-liquid behavior in $Ba(Fe_{1-x}Co_x)_2As_2$. *Phys. Rev. Lett.* **103**, 057001 (2009).
50. Fang, L. et al. Roles of multiband effects and electron–hole asymmetry in the superconductivity and normal-state properties of $Ba(Fe_{1-x}Co_x)_2As_2$. *Phys. Rev. B* **80**, 140508 (2009).
51. Kasahara, S. et al. Evolution from non-fermi- to fermi-liquid transport via isovalent doping in $BaFe_2(As_{1-x}P_x)_2$ superconductors. *Phys. Rev. B* **81**, 184519 (2010).
52. Badoux, S. et al. Change of carrier density at the pseudogap critical point of a cuprate superconductor. *Nature* **531**, 210–214 (2016).
53. Klingeler, R. et al. Local antiferromagnetic correlations in the iron pnictide superconductors $LaFeAsO_{1-x}F_x$ and $Ca(Fe_{1-x}Co_x)_2As_2$ as seen via normal-state susceptibility. *Phys. Rev. B* **81**, 024506 (2010).
54. Zhang, G. M. et al. Universal linear-temperature dependence of static magnetic susceptibility in iron pnictides. *Europhys. Lett.* **86**, 37006 (2009).
55. Shimojima, T. et al. Pseudogap formation above the superconducting dome in iron pnictides. *Phys. Rev. B* **89**, 045101 (2014).
56. Moon, S. J. et al. Infrared measurement of the pseudogap of P-doped and Co-doped high-temperature $BaFe_2As_2$ superconductors. *Phys. Rev. Lett.* **109**, 027006 (2012).
57. Lee, S. et al. Nature of charge density wave in kagome metal ScV_6Sn_6. Preprint at https://arxiv.org/abs/2304.11820 (2023).
58. Kang, S.-H. et al. Emergence of a new band and the Lifshitz transition in kagome metal ScV_6Sn_6 with charge density wave. Preprint at https://arxiv.org/abs/2302.14041 (2023).
59. Canfield, P. C., Kong, T., Kaluarachchi, U. S. & Jo, N. H. Use of frit-disc crucibles for routine and exploratory solution growth of single crystalline samples. *Philos. Mag.* **96**, 84–92 (2016).
60. Blaha, P. et al. WIEN2K: an APW+lo program for calculating the properties of solids. *J. Chem. Phys.* **152**, 074101 (2020).
61. Perdew, J. P., Burke, K. & Ernzerhof, M. Generalized gradient approximation made simple. *Phys. Rev. Lett.* **77**, 3865–3868 (1996).
62. Kawamura, M. Fermisurfer: Fermi-surface viewer providing multiple representation schemes. *Comput. Phys. Commun.* **239**, 197–203 (2019).
63. Rourke, P. & Julian, S. Numerical extraction of de Haas–van Alphen frequencies from calculated band energies. *Comput. Phys. Commun.* **183**, 324–332 (2012).

ACKNOWLEDGEMENTS

This material synthesis and transport experiments performed at the University of Washington are supported by the Air Force Office of Scientific Research under grant FA9550-21-1-0068, the David and Lucile Packard Foundation, and the Gordon and Betty Moore Foundation's EPiQS Initiative, grant no. GBMF6759 to J.-H.C. This material is based upon work supported by the National Science Foundation Graduate Research Fellowship Program under Grant No. DGE-2140004. Any opinions, findings, and conclusions, or recommendations expressed in this material are those of the authors and do not necessarily reflect the views of the National Science Foundation. L.K. and Y.L. are supported by the U.S. Department of Energy, Office of Science Early Career Research Program through the Office of Basic Energy Sciences, Division of Materials Sciences and Engineering. Ames Laboratory is operated for the U.S. Department of Energy by Iowa State University under Contract No. DE-AC02-07CH11358.

AUTHOR CONTRIBUTIONS

J.M.D., E.R., O.P., and Z.L. conducted the transport measurements. Y.L. and L.K. performed the DFT calculations. Q.J. assisted with data analysis. J.M.D. and O.P. grew the samples. J.-H.C. oversaw the project. J.M.D., E.R., and J.-H.C. wrote the manuscript with input from all authors.

COMPETING INTERESTS

The authors declare no competing interests.

ADDITIONAL INFORMATION

Supplementary information The online version contains supplementary material available at https://doi.org/10.1038/s41535-023-00600-8.

Correspondence and requests for materials should be addressed to Jiun-Haw Chu.